Superhyperfine induced photon-echo collapse of erbium in Y_2SiO_5

B. Car,[1] J.-L. Le Gouët,[1] and T. Chanelière [2]

[1]*Laboratoire Aimé Cotton, CNRS, Université Paris-Sud, ENS-Cachan, Université Paris-Saclay, 91405 Orsay, France*
[2]*Univ. Grenoble Alpes, CNRS, Grenoble INP, Institut Néel, 38000 Grenoble, France*

We investigate the decoherence of Er^{3+} in Y_2SiO_5 at low magnetic fields using the photon-echo technique. We reproduce accurately a variety of the decay curves with a unique coherence time by considering the so-called superhyperfine modulation induced by a large number of neighboring spins. There is no need to invoke any characteristic time of the spin fluctuations to reproduce very different decay curves. The number of involved nuclei increases when the magnetic is lowered. The experiment is compared with a model associating 100 surrounding ions with their exact positions in the crystal frame. We also derive an approximate spherical model (angular averaging) to interpret the main feature the observed decay curves close to zero field.

I. INTRODUCTION

The interest for rare-earth doped materials has been recently renewed by the quest for quantum technology devices. The longest coherence times are generally observed in non-Kramers ions (even number of electrons) because their spins possess a nuclear spin character in low symmetry site as the emblematic europium in Y_2SiO_5 [1]. The research activity on Kramers ions has been maintained, despite the generally lower coherence times, because they cover an interesting wavelengths panel in the infrared region. Erbium holds a lot of promises in that sense because of the compatibility with the optical fiber communication range. The large electron spin undeniably induces decoherence but offers also significant advantages that have been reconsidered for quantum information processing. The electron spin resonance (ESR) falls in the GHz range, an actively investigated region to operate superconducting qubits, allowing a hybridization between quantum circuits and spin ensembles [2]. The apparently detrimental spin sensitivity appears as a major benefit when a very low number of spins is targeted [3]. The interplay between optics and microwave is fully exploited by the scheme of coherent frequency conversion. Indeed, the transduction of quantum states from the microwave to the optical domain appears as a missing link in the quantum technology landscape [4,5]. The potential of Kramers ion has been rapidly identified in this context [6].

We focus on the low magnetic field region, typically below 100 mT. This offers fundamental interests beyond the experimental advantage of using smaller magnets. First, the phonon density is small at cryogenic temperature (2–4 K). Second, the ESR transitions (potentially involving the hyperfine structure) fall in the few GHz range and are then directly compatible with superconducting high-Q resonators [4,5]. Early demonstrations have already involved Er^{3+} : Y_2SiO_5 [7]. Optical spin excitation can also be obtained conveniently with a single laser modulated with modern electro-optics devices. Many experiments are performed close to zero field in practice with Er^{3+} or Yb^{3+} for example [8–11].

Despite a clear interest for low magnetic field region, the variation of the coherence time is essentially unexplored. One has the tendency to dodge the issue by noting that echos exhibit strong superhyperfine modulations induced by neighboring ligands nuclei (sometimes called ligands interaction) making a complete analysis difficult because of the diversity of modulation patterns. In any case, the erratic nature of the measurements disappears close to zero field where modulations are absent and the decay (exponential or not) is extremely rapid although one does not expect any change in the spin bath dynamics. This coherence collapse may give the impression that a sudden change of regime is happening. This is not the case. We will give a unified vision of the decoherence at low field without invoking any change in the spins dynamics and precisely explain the collapse of the measured coherence time when field is reduced. Our analysis is based on the superhyperfine coupling exclusively [12]. Again, we do not consider the ligand nuclear flip flops nor the electron spin flip flops that induce a magnetic noise and affect the coherence time of the impurity. We investigate a different mechanism, static in the sense that we neglect the spin dynamics.

We consider a large collection of yttrium surrounding an Er^{3+} center. They all have different couplings to the dopant electron spin because of the distance and the anisotropy of the Er^{3+} dipolar field. The sudden excitation by the brief echo measurement pulses of those multiple frequencies leads to an *apparent* decay time that is much shorter that the coherence time induced by the background spin flip flops observed at a larger field [1,13,14]. This phenomenon has been discussed early for ESR transitions [14,15]. It explains the shortness, literally the collapse of the measured dephasing times for the different Kramers ion (including Er^{3+}) at zero field [13].

Although early predicted in ESR [14,15] as an extreme case of envelope modulation, the superhyperfine nuclear induced decay regime is rarely observed in practice, because the experiments are usually performed in the radio-frequency X-band (~9 GHz). In that case, the magnetic field is

already sufficiently large (>100 mT) to dominate the electron spin dipolar field [16], so the superhyperfine modulations are weakly contrasted (but visible in the Fourier spectrum). Custom-made ESR spectrometers with a variable resonant frequency are clearly more adapted [17]. Optical techniques are intrinsically broadband and can be implemented close to zero field without modification of the laser setup [18,19]. Using the photon-echo technique, we show that the rapid decoherence of Er^{3+} : Y_2SiO_5 is well explained by the static superhyperfine interaction with a collection of yttrium ions.

Historically, the superhyperfine interaction between a Kramers ion and the ligand nuclei has been widely studied starting from the seminal work of Mims on Ce^{3+} in $CaWO_4$ [20]. It has been also evidenced later on in Er^{3+} : Y_2SiO_5 using standard ESR techniques [16] or superconducting resonators [21]. Optical and RF measurements have allowed us to characterize the superhyperfine interaction in a variety of host crystals as YVO_4 with Yb^{3+} and Nd^{3+} [22,23], $YLiF_4$ with Nd^{3+} and Er^{3+} [24,25], or $CaWO_4$ with Er^{3+} exhibiting a remarkably high sensitivity [17].

Concerning Er^{3+} : Y_2SiO_5 because of the perspectives in classical and quantum processing, advanced spectroscopic studies have been used to accurately describe the dopant in the crystal field [26,27], the different g tensors (in both substitution sites of yttrium and in the ground and optically excited state of Er^{3+}) [28]. The hyperfine tensors for odd isotopes are also known [29,30]. This abundant literature is essential to describe the superhyperfine coupling. In this study, we crudely extract the Y^{3+} positions from the crystal structure [31] and calculate the couplings one by one generalizing our previous approach in Ref. [19].

The paper is organized as follows. We first describe the experimental apparatus and show typical photon-echo decay curves between 0 and 133 mT. We analyze the curves by extending the envelope modulation model to a cluster of 100 surroundings yttrium ions. We show that for a decreasing magnetic field, the number of coupled nuclei increases. We finally interpret the low-field collapse by assuming an equivalent homogeneous spherical distribution of yttrium around the rare-earth ion. This allows us to reproduce the main feature of the observed decay curve and to introduce the notion of an inflating sphere of influence of the Er^{3+} ion when the magnetic field is reduced.

II. EXPERIMENT

We perform two-pulse photon echo measurements on the

$$^4I_{15/2} \rightarrow {}^4I_{13/2}$$

transition of Er^{3+} in Y_2SiO_5. The configuration is very similar to our previous study of the superhyperfine coupling with a single nucleus [19]. As a reference frame for the magnetic field orientation, we use the optical frame (D_1, D_2, b) [26,31] where D_1 and D_2 are the extinction axes. This is a natural frame for optical measurements. Additionally, the axes are perpendicular as opposed to the monoclinic crystal frame.

We roughly orientate the magnetic field B in the (D_1, D_2) plane at 50° from D_1 by rotating the crystal in the magnet close to the previously studied configuration [19]. Staying in the (D_1, D_2) plane simplifies the analysis because the so-
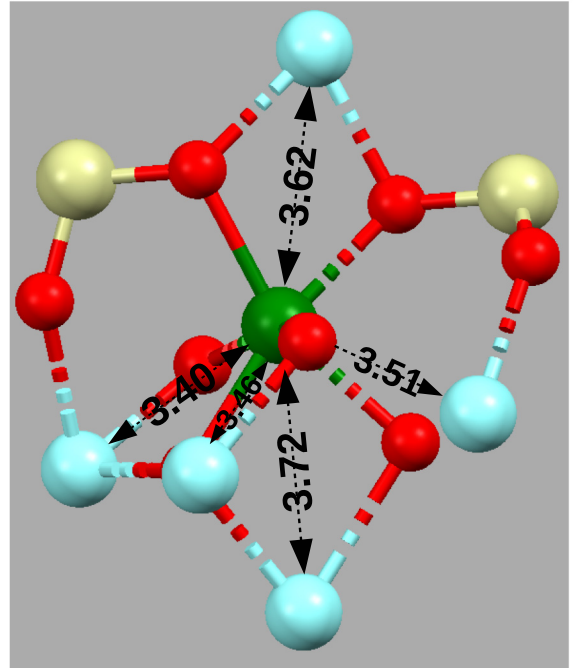

FIG. 1. Reduced crystal cell representing site 1 in the Y_2SiO_5 matrix: Erbium in green substitutes a yttrium in the six-coordinate site. Color code: cyan—yttrium, red—oxygen, and yellow—silicon. The yttrium ions are the five nearest neighbors with distances 3.40 Å, 3.46 Å, 3.51 Å, 3.62 Å, and 3.72 Å from the erbium center. The distances of the two represented silicons are 3.26 Å and 3.51 Å.

called magnetic subsites (related by a C_2 symmetry about b) are equivalent. This aspect will be discussed in Appendix B.

We optically resolve the lowest to lowest spin state transition of site 1 (at 1536.38 nm, see Fig. 1 for a cell representation) allowing a well defined orientation of the Er^{3+} magnetic moment in both ground and excited states. We will also take data at zero field (by zeroing the magnet current) where this assumption fails. This aspect will be discussed in Sec. IV. The sample is lightly doped (10 ppm, grown by Scientific Materials Corporation) to avoid the so-called erbium spin flip flops that may perturb the echo decay curve (in the regime of small magnetic fields [32]). We cool down the crystal to 1.8 K. The light propagates along the b axis of the crystal and the polarization is parallel to D_2 to maximize the absorption and the photon-echo signal.

In the following, we neglect the response of the ^{167}Er isotope (22% of the dopant concentration, with a nuclear spin of 7/2) that is broadly spread over a large amount of possible hyperfine transitions [29] and therefore can be neglected because of the optical selection [19]. Concerning the nuclear spins present in the matrix, ^{89}Y is the most abundant (100% natural abundance with a 2.1 MHz/T nuclear magnetic moment). ^{29}Si is also present with 4.7% abundance and a 8.5 MHz/T magnetic moment [33]. It is important to keep in mind that the natural abundance scales the modulation contrast which cannot be larger than 4.7% for ^{29}Si [34]. In any case, the ^{29}Si nuclear modulations are typically ~20 times weaker than the ^{89}Y. Additionally, because of a larger magnetic moment, ^{29}Si nuclear modulations would appear at a four times larger frequency (as
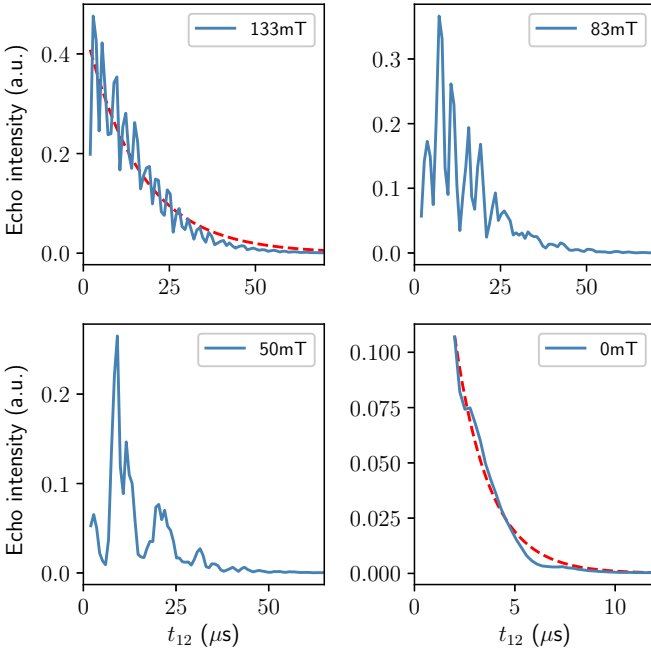
FIG. 2. Echo decay curves for $B = 133$, 83, 50, and 0 mT exhibiting different modulation patterns. We fit data by an exponential decay (red dashed line) for $B = 133$ and 0 mT and find decay times of 63 μs and 6.9 μs, respectively. The meaning of theses characteristic times will be discussed in details.

the ratio of nuclear moments) making them difficult to observe at our measurement time scale. That is the reason why we focus on yttrium nuclei exclusively in the following.

We plot the decay curve of the photon-echo signal as a function of t_{12}, the delay between the two pulses, for different values of the magnetic field (see Fig. 2). It is important to note that we cannot obtain the echo intensity for $t_{12} <$ 2 μs because the signal is overwhelmed by the strong pulse free-induction decay. At $B = 133$ mT, the envelope ($\sim$63 μs decay time) is clearly modulated. Below this value, the pattern is erratic. At $B = 0$ mT, we retrieve a smoother but faster decay curve which could be interpreted as an exponential decay at first sight with a characteristic time of 6.9 μs. These characteristics have been already reported in the literature even if the intermediate region (between 0 and 100 mT) is usually not considered because of the erratic aspect of the curves and the difficulty to model the envelope modulation. We will tackle this problem and fit data by assuming a single value of coherence time, common to the different curves (from 0 and 133 mT in our case).

III. MODEL

As discussed in the introduction, we won't consider the spin dynamics that induce decoherence on a longer timescale that the one we observe at larger fields. This T_2 is an upper limit of our echo decay time. As we will discuss later, there is no reason for the T_2 to vary within our measurement range. On a shorter timescale, the echo decay is driven solely by the superhyperfine coupling with a multiplicity of Y^{3+} ions. To reproduce the experimental photon-echo curves, we need

to account for a collection of surrounding yttrium ions. The difficulty in Y_2SiO_5 comes from the low symmetry of the host matrix. Indeed when the Er^{3+}- Y^{3+} interactions are considered, the different positions of the surrounding yttrium ions do not exhibit a symmetrical structure that would simplify the analysis. Nevertheless, since the Y^{3+} positions is known from the crystal structure [31], one can add their contributions using the historical ESR formula [34,35]. This is sufficient to obtain a very satisfying theoretical agreement. This approach has also been successful to describe ESR in glassy materials, with a profusion of disordered sites, which exhibit less contrasted modulations or even rapid decays induced by the multiple modulation frequencies which can still be used to extract a characteristic coupling [34,36]. This work is a substantial basis for our analysis. The change of the electron spin dipole moment orientation between ground and excited state of the Er^{3+} center modifies the magnetic field seen by given Y^{3+} ions. The modulation comes from the electron-nuclear spin mixing excited during the echo sequence. For multiple coupled nuclei, the envelope modulation is obtained as a product of single superhyperfine modulations:

$$\mathcal{V}_{\text{tot}} = \prod_i \mathcal{V}_i, \qquad (1)$$

where $\mathcal{V}_i$ is the modulation due to the yttrium numbered i which reads as

$$\mathcal{V}_i(t_{12}) = 1 - \frac{\rho_i}{2}[1 - \cos(\Delta_i t_{12})][1 - \cos(\Delta'_i t_{12})], \qquad (2)$$

where ρ_i is the branching contrast (using the terminology developed in Ref. [19]), Δ_i and Δ'_i the superhyperfine splittings in the ground and excited states of erbium, respectively (lowest spin states of $^4I_{15/2}$ and $^4I_{13/2}$). This gives the modulation of the echo field. As we measure the intensity (as opposed to ESR), the decay should be proportional to

$$[\mathcal{V}_{\text{tot}}(t_{12})]^2 \times \exp\left(-\frac{4t_{12}}{T_2}\right), \qquad (3)$$

including an exponential decoherence decay and the superhyperfine modulations. A calculation of the parameters ρ_i, Δ_i, and Δ'_i in Eq. (2) has been detailed in Ref. [19] for a given yttrium position, a given orientation, and magnitude of the magnetic field. This calculation will be briefly summarized as a reminder in Appendix B. We consider a cluster of 100 nearest yttriums positioned in the crystal frame [31] and repeat the calculation for each ion i to evaluate $\mathcal{V}_{\text{tot}}$ [Eq. (1)]. Each experimental curve can then be fitted by Eq. (3). Per curve, there are only two fitting parameters: a vertical scaling factor (normalization) and the T_2 value. The term $[\mathcal{V}_{\text{tot}}(t_{12})]$ is completely fixed by the magnetic field and the tabulated yttrium positions.

One can even further constraint the fitting parameters by keeping the same value of the coherence time T_2 within our measurement range 0–133 mT. The T_2 is induced by the background spin flip flops (electronic or nuclear depending on the dopant concentration) that should not vary much in our case. For our magnetic field orientation, the maximum electron spin Zeeman splitting is $\sim$9 GHz in the ground state at 133 mT (with a g factor of 4.8 for this orientation), still much smaller than the temperature (1.8 K $\sim$ 36 GHz). In
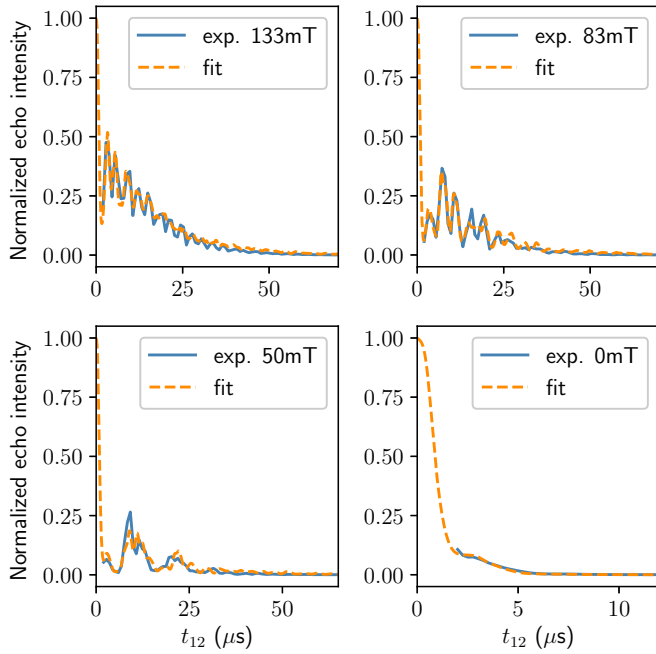
FIG. 3. Echo decay curves of Fig. 2 (blue line) superimposed with the theoretical formula Eq. (3) (orange dashed line). The coherence time is the same, $T_2 = 58\ \mu$s.

the absence of net spin polarization, the Er^{3+} flip-flop rate should not change. The nuclear spins are even less affected by such a weak magnetic field. So the spin dynamics as a whole is essentially unchanged in our range and as a consequence, the T_2 should be constant. So we keep the T_2 as a free fitting parameter but constrained to be the same for all the curves in the measurement range. We simply introduce a factor of normalization (scaling) between each theoretical and experimental curve.

The match is very satisfactory (see Fig. 3 and the complementary measurements in Appendix A). We reproduce well the different modulation patterns. The theoretical curves serve as normalization and equal 1 at $t_{12} = 0$. All the fitting curves share the same coherence time value $T_2 = 58\ \mu$s despite the disparity of decay patterns. Because we cannot measure the echo intensity for $t_{12} < 2\ \mu$s, we miss a very rapid decay (at the μs timescale) that is well predicted by Eq. (3). At zero field, despite the precautions that should be taken when the magnet current goes to zero (see Sec. IV), what we interpret as an *apparent* 6.9 μs decay in Fig. 2 seems to be the result of the superhyperfine modulations acting on a much longer T_2 decay. We interpret this discrepancy at low field between the decoherence and the *apparent* times as the interaction with the increasing number of coupled nuclei.

IV. QUALITATIVE INTERPRETATION

The superhyperfine induced decay can be interpreted by reconsidering Eq. (2) for the different yttriums. We plot the key parameters ρ_i, Δ_i, and Δ'_i as a function of the distance from the electron spin in Fig. 4.

The curves appear erratic because of the superhyperfine interaction anisotropy. Indeed, for the same distance, certain
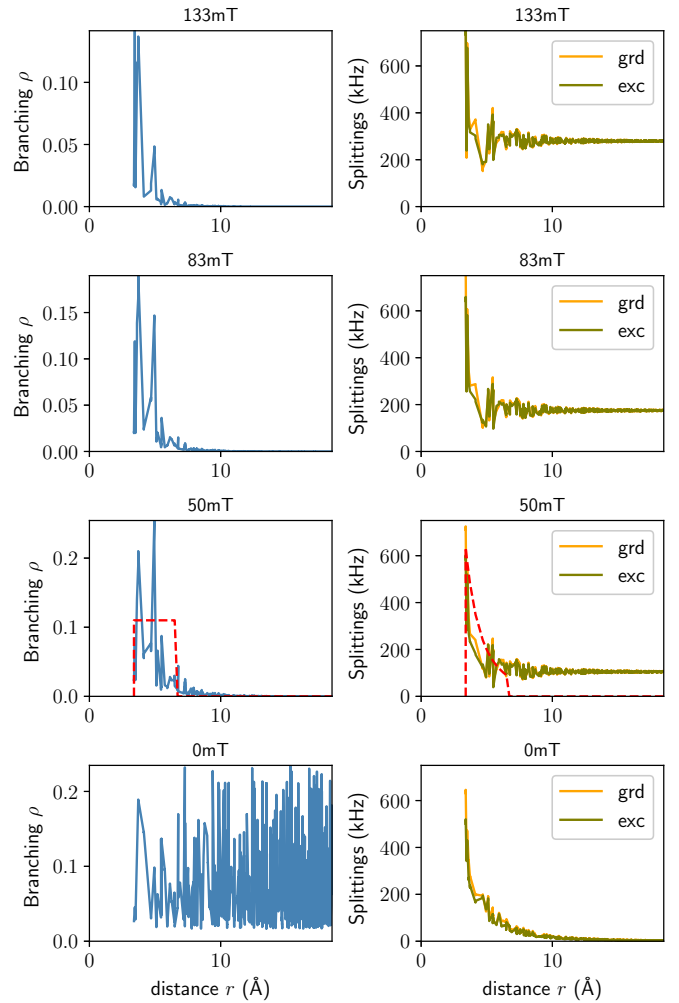

FIG. 4. We plot the modulations parameters ρ_i (left), Δ_i (right, orange), and Δ'_i (right, green) as a function of the nucleus distance from the dopant for the different values of the magnetic field previously considered. We here represent 500 ions ranging 3.4 Å (nearest neighbor distance) to 18.5 Å. As a reminder, in modeling Fig. 3, we only use 100 ions (from 3.4 Å to 8.6 Å). The red dashed lines at 50 mT serve for the approximate spherical model that will be discussed in Sec. V where we assume an effective constant branching contrast (50 mT, left) and a truncated dipolar splitting decay (50 mT, right).

yttriums have very different angular coordinates, so they may have very different splittings. Despite the irregular nature of the branching contract (left column of Fig. 4) and the splittings (right column of Fig. 4), the plots can be analyzed as follows. The total magnetic field contains two contributions. First, the dipolar field generated by the Er^{3+} which globally decreases as $1/r^3$ (neglecting the orientational dependency in a first approach). Second, the constant bias field so the splittings tend asymptomatically at large distances to the nuclear spin Zeeman splitting (2.1 MHz/T) whatever the dopant in the ground or excited state. The branching contrast can only be significant if the dipolar field dominates the bias field [19,37] (see also Appendix B 1). In a sense, the bias magnetic field screens the area of influence of electron spin. At a certain

distance, the magnetic field becomes larger than the Er^{3+} dipolar field, so the branching of distant yttriums is very weak.

One could for example define a screening radius within which the Er^{3+} field dominates the bias field and leads to a large branching contrast. The broadband excitation of the Y^{3+} ions under the influence of Er^{3+} (namely with a significant branching contrast) explains the collapse of the echo signal. The number of yttriums increases as the magnetic field is reduced (thus reducing the screening). This will be discussed quantitatively in Sec. V.

At the extreme, the sphere of influence covers the whole space as the magnetic field goes to zero. The number of nuclei diverges with a relatively low average branching value (typically ~0.1 with large fluctuations). Even though there is no singularity in the modulation pattern because the splittings decay rapidly by following a $1/r^3$ law (at 0 mT, see Fig. 4).

As mentioned earlier, we have extended the results of our model to 0 mT in Fig. 4 with a satisfying agreement with the data set in Fig. 3. Nonetheless, this zero-field analysis should be handled with precaution. In our model, we indeed assume that the lowest spin states of $^4I_{15/2}$ and $^4I_{13/2}$ are selectively addressed. The magnet current is reduced to zero to obtain the 0 mT curve. The spin state transitions are not optically resolved anymore, so our model doesn't strictly apply. In any case, the expectation values of the Er^{3+} dipole moment are only well defined (see Appendix B for details) if the magnetic field is present to align the spins. Even when the magnet current is reduced to zero, one cannot exclude the presence of a remanent field because of a magnetization of the sample holder parts or the earth magnetic field. Nevertheless, there is no reason for this remanent field to be aligned with the bias magnetic field used in Sec. III. So the extension of the model for a given dipole moment orientation at zero field and the fortunate agreement with the measurement should deserve more investigations.

V. APPROXIMATE SPHERICAL MODEL

The goal of this section is to move away from the accurate heavy calculations and to give some physical content to the different parameters, primarily ρ_i, Δ_i, and Δ_i' in Eq. (2). There are two features that we would like to put forward by focusing on one set of data in Fig. 3 at 50 mT. First, the rapid initial decay time is a consequence of quasicontinuum of superhyperfine splittings when a large Y^{3+} ensemble is excited by the echo sequence. Second, at low fields, the decay curves exhibit a series of revivals, that cannot be qualified as a pure oscillation, as observed in Fig. 3 at 50 mT (two revivals between $t_{12} = 0$ and 25 μs) and in the complementary measurements in Fig. 6 at 17 mT (a single revival in the range $t_{12} \sim 25$ μs). Both aspects can be addressed analytically by introducing a continuous distribution of superhyperfine splittings and defining a Er^{3+} sphere of influence whose radius depends on the magnetic field as we will see now.

As discussed qualitatively in Sec. IV, we observe that the dipolar field globally decreases as $1/r^3$ in both ground and excited states up to a point where it is dominated by the bias field (so the splittings tend to the nuclear Zeeman values). This defines a screening radius for the Er^{3+} dipolar field. We can then make a crude assumption. Let's assume

that all the nuclei for which the dipolar field dominates the bias magnetic field have a nonzero branching contrast. On the contrary, when the bias field dominates, the branching is zero. This defines a hard sphere of influence of the Er^{3+} ion. In other words, out of a certain screening radius, Y^{3+} are assumed completely decoupled from the electron spin. The Er^{3+} ground and excited dipolar fields cannot be strictly equal otherwise the branching contrast would be zero [19,37] (see also Appendix B 1). In other words, the ground and excited dipolar fields are equal to the lowest order but slightly misaligned to generate a weak branching contrast to the first order as observed in Fig. 4 (50 mT) with $\rho_i \ll 1$.

In practice, we write the splittings of the Y^{3+} numbered i at the distance r as $\Delta_i \simeq \Delta_i' \simeq \bar{\Delta}$ which follows the $1/r^3$ decay law as

$$\bar{\Delta}(r) = \Delta_0 \frac{r_0^3}{r^3}, \tag{4}$$

where $r_0 = 3.4$ Å, the nearest neighbor distance and Δ_0 the corresponding splitting. We then assume the branching contrast to be constant $\rho_i \simeq \bar{\rho}$ up to the screening radius r_S and zero elsewhere for $r_i > r_S$.

We will keep Δ_0, $\bar{\rho}$, and r_S as free parameters for the approximate model. Nevertheless, we expect Δ_0 and $\bar{\rho}$ to be of the order of $\Delta_0 \sim 2\pi \times 600$ kHz and $\bar{\rho} \sim 0.1$ as observed in Fig. 4 (50 mT). Concerning the screening radius r_S, we expect that the dipolar splitting $\bar{\Delta}(r_S)$ at the distance r_S defined as

$$\bar{\Delta}(r_S) = \Delta_0 \frac{r_0^3}{r_S^3} = \Delta_S \tag{5}$$

to be of the order of $\frac{\mu_Y}{h}B$ with μ_Y/h the Y^{3+} nuclear (isotropic) dipole moment (expressed in Hz/T). In other words, r_S corresponds to a compensation between the dipolar field and the bias field B.

The superhyperfine modulation envelope can now be evaluated. Equation (3) can be simplified when the branching contrast is small as

$$[\mathcal{V}_{\text{tot}}(t_{12})]^2 \simeq \exp\left(-\sum_i \bar{\rho}[1 - \cos(\Delta_i t_{12})]^2\right). \tag{6}$$

The discrete sum is replaced by a continuous integral in the spherical model:

$$[\mathcal{V}_{\text{tot}}(t_{12})]^2 \simeq \exp\left(-\int_{r_0}^{r_S} \bar{\rho}[1 - \cos(\bar{\Delta}(r)t_{12})]^2 4\pi r^2 n_Y dr\right), \tag{7}$$

where $n_Y = 1.83.10^{22}$ at/cm^3 is the yttrium density. The expected modulation pattern calculated as a continuous integral in Eq. (7) is truncated to r_S where the branching contrast is assumed to be zero.

The superhyperfine decay can be rewritten as

$$\exp\left(-\frac{8\pi}{3}n_Y r_0^3 \bar{\rho}\Delta_0 t_{12}\int_{\Delta_S t_{12}/2}^{\Delta_0 t_{12}/2}\frac{\sin^4\phi}{\phi^2}d\phi\right) \tag{8}$$

using the change of variable $\phi = (\Delta_0 t_{12}/2)\frac{r_0^3}{r^3}$ where we have introduced the value of Δ_S defined in Eq. (5). The integral term $\int_{\Delta_S t_{12}/2}^{\Delta_0 t_{12}/2}\frac{\sin^4\phi}{\phi^2}d\phi$ oscillates as a function of t_{12} and modu-
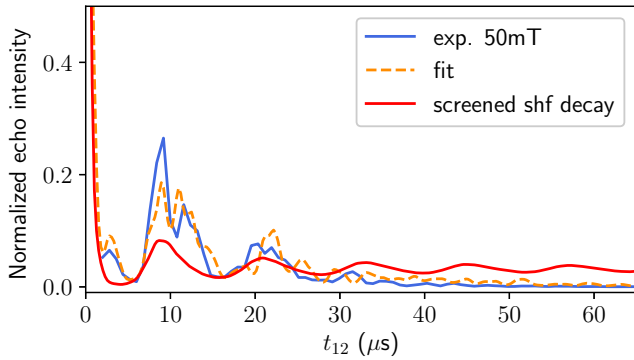
FIG. 5. Revivals of the echo decay (blue line) at 50 mT [as in Fig. 3, the orange dashed line is the theoretical formula Eq. (3)]. The qualitative shape is reproduced by introducing a screening of the superhyperfine interaction in Eq. (8) (screened superhyperfine decay in red line, see text for analysis).

lates the exponential decay term given by $\frac{8\pi}{3} n_Y r_0^3 \bar{\rho} \Delta_0 t_{12}$. In a sense, the latter gives a characteristic decay time of $\frac{3}{8\pi n_Y r_0^3 \bar{\rho} \Delta_0}$.

This expression can phenomenologically reproduce the oscillating decay curve at 50 mT. To do so, we leave Δ_0, Δ_S, and $\bar{\rho}$ as free parameters and fit the experimental data (blue line in Fig. 3, 50 mT). The agreement in Fig. 5 is qualitatively satisfying.

The best fit gives reasonable values of $\Delta_0 = 2\pi \times$ 635 kHz and $\Delta_S = 0.8 \frac{\mu_Y}{h} B$ for the screening splitting, and $\bar{\rho} = 0.11$ for the contrast as expected from the analysis of Fig. 4 (50 mT). More importantly, the value $\Delta_S = 0.8 \frac{\mu_Y}{h} B$ corresponds well to our expectation. When the splittings are larger than Δ_S, the dipolar field coarsely dominates the nuclear Zeeman term. This is the way we have defined the screening sphere of the Er^{3+} influence. From Δ_S, we can extract the value of the screening radius $r_S = 6.7$ Å using Eq. (5). This should be compared to $r_0 = 3.4$ Å, the nearest neighbor distance.

Equation (5) is plotted with the fitted parameters in Fig. 4 (50 mT, right column, dashed red line) for comparison with the accurate model of Sec. III between $r_0 = 3.4$ Å and $r_S = 6.7$ Å. The fitted value of the branching $\bar{\rho} = 0.11$ is also represented in Fig. 4 (50 mT, left column, red dashed line). Theses effective values of the splittings and the branching contrast allow us to reproduce satisfyingly our case of study at 50 mT.

As the magnetic field is increased, the radius decreases thus reducing the number of interacting nuclei. This justifies the need to apply a minimal magnetic field. Indeed, the superhyperfine induced decay regime can be eliminated by increasing the field to a point where the screening radius is comparable to r_0 so a very limited number of Y^{3+} are still interacting. Additionally, when a few ions are in the Er^{3+} area of influence, the anisotropy of the electron spin can be used to turn on or off the interaction with isolated nuclei [19].

VI. CONCLUSION

We have used the photon-echo technique to investigate the decoherence of $Er^{3+} : Y_2SiO_5$ at low field. The collapse of

the coherence time is not due to a modification of the electron or nuclear spins dynamics that is essentially unaffected at low field. Instead, the decay curves are accurately explained by the superhyperfine modulations that involve an increasing number of nuclei as the field is reduced. The low-field decay can be reproduced analytically by considering a spherical model (angular averaging) and introducing a cutoff of the Er^{3+} dipolar field, thus defining a screening radius of the electron spin influence.

The term decoherence for the superhyperfine induced collapse is actually questionable. During the *true* coherence time, $T_2 = 58$ μs in our case, the evolution of the spin ensemble (Er^{3+} and a large collection of nuclei) is indeed unitary and potentially reversible. This is a striking feature of the mesoscopic ensemble evolution (cluster of Y^{3+} around Er^{3+}). One may wonder if the rapid superhyperfine decay can be canceled thus exploiting the reversibility of the process. There is no obvious solution except extending the pulse duration or reducing the power to perform a spectral selection [38–40]. This is an interesting approach to gain understanding on the system but this constrains the *apparent* decay to the experimental parameters (pulse duration for example).

This doesn't necessarily mean that the superhyperfine induced collapse should be considered as a hard limit. One could on the contrary consider the repetition of short pulses to compensate for the dephasing induce by the inhomogeneous superhyperfine couplings. Despite a clear analogy with the dynamical decoupling technique, the term dynamical is not appropriate because the *apparent* decay is not driven by the dynamical fluctuations of the environment. Additionally, the transposition of this RF technique to the optical domain is not direct because repeated coherence refocusing would trigger the emission of multiple photon echoes. Still, our analysis shows that the application of sub-μs pulses would compensate for the superhyperfine collapse. They are not technically accessible in our case because a large peak power is needed to maintain a significant pulse area. This nevertheless draws a stimulating perspective to compensate for the superhyperfine coupling to a large nuclear spin ensemble at low field.

APPENDIX A: COMPLEMENTARY MEASUREMENTS

We complement the experimental measurements of Fig. 2 with different magnetic field values. The fitting procedure was explained in Sec. III, so Fig. 6 is analogous to Fig. 3. All the curves (Figs. 3 and 6) are fit with a unique coherence time $T_2 = 58$ μs.
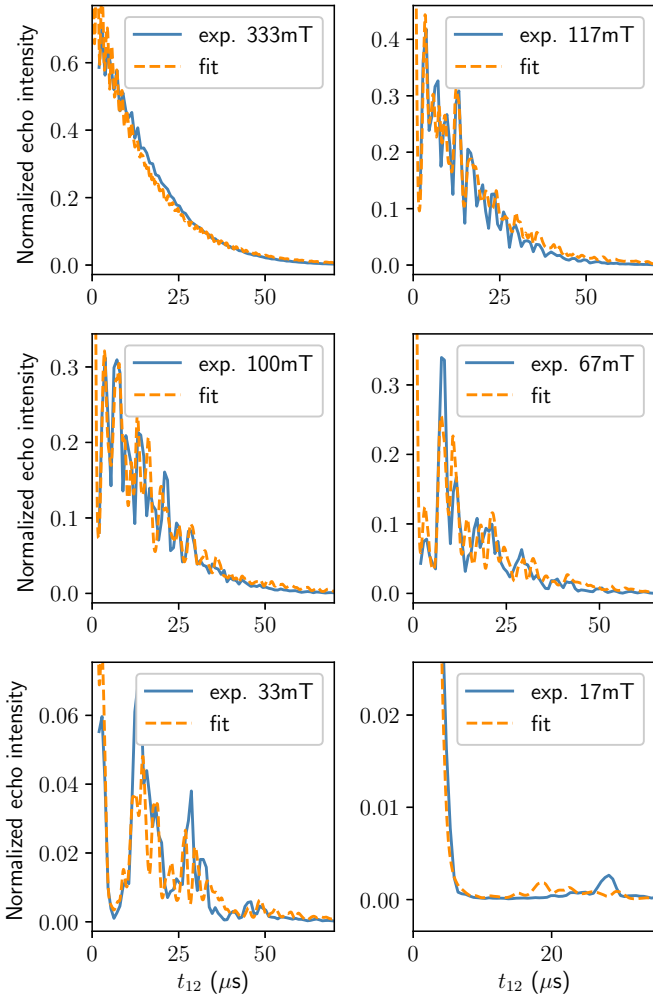
FIG. 6. Complementary experimental measurements echo decay curves (blue line) with different magnetic field values than Fig. 2. As in Fig. 3, we have superimposed the theoretical formula Eq. (3) (orange dashed line). The fit is normalized to one at $t_{12} = 0$. We have adjusted the vertical scale to draw the attention on the experimental data.

APPENDIX B: CALCULATION OF THE MODULATION PARAMETERS

We first remind the general reasoning to calculate the modulation parameters of Eq. (2) in Appendix B 1. The calculation has been already detailed in Ref. [19]. We also treat the inequivalent site orientations, sometime called magnetic subsites, present in the Y_2SiO_5 matrix. The fit agreement in Fig. 3 is obtained when the magnetic doesn't exactly lie in the (D_1, D_2) plane but slightly offset. In that case, the two possible site orientations (called orientations I and II in Ref. [28] and related by a C_2 rotation about b) are not equivalent and have to be treated independently (see Appendix B 2).

1. General approach

For a given Y^{3+} spin whose location is $\boldsymbol{r}$ referenced from the dopant, the effect of the Er^{3+} electron spin can be treated

in a perturbative manner by introducing the Hamiltonian

$$H'_{g,e} = -\boldsymbol{\mu}_Y \cdot \boldsymbol{B}_{g,e}(\boldsymbol{r}) \quad \text{(B1)}$$

depending if the Er^{3+} is in the ground or the optical excited state (written with subscripts g or e), respectively [19]. $\boldsymbol{\mu}_Y$ is the Y^{3+} nuclear (isotropic) dipole moment. The field

$$\boldsymbol{B}_{g,e}(\boldsymbol{r}) = \boldsymbol{B} + \boldsymbol{B}_{g,e}^{Er}(\boldsymbol{r}) \quad \text{(B2)}$$

is the total magnetic field seen by the Y^{3+} ion including the bias field $\boldsymbol{B}$ and the dipolar field generated by the Er^{3+} spin at the location $\boldsymbol{r}$ of the nuclear spin. The latter takes the general form

$$\boldsymbol{B}_{g,e}^{Er} = -\frac{\mu_0}{4\pi} \left[\frac{\langle \boldsymbol{\mu}_{g,e}^{Er} \rangle}{r^3} - 3 \frac{\left(\langle \boldsymbol{\mu}_{g,e}^{Er} \rangle \cdot \boldsymbol{r} \right) \cdot \boldsymbol{r}}{r^5} \right], \quad \text{(B3)}$$

where $\langle \boldsymbol{\mu}_{g,e}^{Er} \rangle$ is the Er^{3+} electron spin dipole moment (expectation value), written $\boldsymbol{\mu} = \langle \boldsymbol{\mu}_g^{Er} \rangle$ (ground) and $\boldsymbol{\mu}' = \langle \boldsymbol{\mu}_e^{Er} \rangle$ (excited) in the text.

This is sufficient to extract the parameters of interest in Eq. (2), namely Δ and Δ' the superhyperfine splittings when the erbium is in the ground or excited state as the eigenvalues of H'_g and H'_e, respectively. Finally, the branching contrast ρ has the simple geometrical interpretation as $\rho = \sin^2(\theta)$ where $\theta = (\boldsymbol{B}_g, \boldsymbol{B}_e)$, the angle between the total magnetic fields.

The dipole moments $\boldsymbol{\mu}$ and $\boldsymbol{\mu}'$ are not aligned with the magnetic field $\boldsymbol{B}$. This is a consequence of the local site anisotropy as revealed by the anisotropy of the g tensor tabulated in Ref. [28] Table III.

2. Considering the two possible magnetic orientations

If the magnetic field $\boldsymbol{B}$ is contained in the (D_1, D_2) plane or parallel to b, then there is no need to bother with the

TABLE I. Y^{3+} positions for orientation I (Å).

Y^{3+} number	Distance r	D_1 coord.	D_2 coord.	b coord.
1	3.40	−0.66	3.23	−0.81
2	3.46	−3.45	0.28	0.00
3	3.51	−1.66	−1.88	2.45
4	3.62	2.27	−2.24	−1.72
5	3.72	−1.79	2.15	2.45
6	4.15	−2.79	−2.95	−0.81
7	4.70	3.93	−0.37	2.55
8	4.95	−1.66	−1.88	−4.27
9	5.10	−1.79	2.15	−4.27
10	5.19	5.06	0.71	−0.91
11	5.46	−1.01	−5.11	1.64
12	5.46	1.01	5.11	1.64
13	5.50	3.27	2.86	−3.36
14	5.50	3.27	2.86	3.36
15	5.74	3.93	−0.37	−4.17
16	5.93	2.27	−2.24	5.00
17	6.14	−2.44	5.38	1.64
18	6.27	2.92	−5.47	−0.91
19	6.48	−5.71	2.52	−1.72
20	6.48	5.71	−2.52	−1.72

two different site orientations because they are equivalent. In short, the magnetic subsites have the same dipoles moments $\boldsymbol{\mu}$ and $\boldsymbol{\mu'}$.

Otherwise, the orientations I and II have to be treated independently. There is no special difficulty. The corresponding g tensors are related by a C_2 rotation about b as tabulated in Ref. [28] Table III. The values of $\boldsymbol{\mu}$ now written $\boldsymbol{\mu}_I$ and $\boldsymbol{\mu}_{II}$ are calculated independently (same for $\boldsymbol{\mu'}$). We do not obtain the same values for $\boldsymbol{B}_g^{Er}$ in Eq. (B3), obviously because the $\boldsymbol{\mu}_I$ and $\boldsymbol{\mu}_{II}$ are different (same for $\boldsymbol{B}_e^{Er}$ with $\boldsymbol{\mu'}$) but also because the relative positions of the surrounding Y^{3+} are different: The C_2 rotation has to be applied to $\boldsymbol{r}$ for each yttrium. We give the explicit positions of 100 ions in C that may serve to the reader for further analysis.

We finally calculate the parameters ρ_i, Δ_i, and Δ_i' in Eq. (2) for an ensemble of 100 ions (labeled i) per orientation and obtain the modulations $\mathcal{V}_{tot}^I$ and $\mathcal{V}_{tot}^{II}$ for each orientation. We sum the two contributions in a coherent manner to evaluate the final ensemble modulation

$$\mathcal{V}_{tot} = \frac{\mathcal{V}_{tot}^I + \mathcal{V}_{tot}^{II}}{2}. \tag{B4}$$

TABLE II. Y^{3+} positions for orientation II (Å).

Y^{3+} number	Distance r	D_1 coord.	D_2 coord.	b coord.
1	3.40	0.66	−3.23	−0.81
2	3.46	3.45	−0.28	0.00
3	3.51	1.66	1.88	2.45
4	3.62	−2.27	2.24	−1.72
5	3.72	1.79	−2.15	2.45
…	…	…	…	…

APPENDIX C: POSITIONS OF THE Y^{3+} IONS

We here give the Y^{3+} positions used to calculate the superhyperfine splittings in orientation I. We write the first 20 ions (sorted by distance from the Er^{3+} center) in Table I. The coordinates are given in the frame D_1, D_2, and b. The complete set of 100 ions used for the calculation is given as Supplemental Material [41] in the form of a text file.

We also give the first five Y^{3+} ions in orientation II in Table II. They are simply deduced from the positions for the other site by a C_2 rotation about b.

[1] M. Zhong, M. P. Hedges, R. L. Ahlefeldt, J. G. Bartholomew, S. E. Beavan, S. M. Wittig, J. J. Longdell, and M. J. Sellars, Nature (London) **517**, 177 (2015).

[2] Y. Kubo, C. Grezes, A. Dewes, T. Umeda, J. Isoya, H. Sumiya, N. Morishita, H. Abe, S. Onoda, T. Ohshima, V. Jacques, A. Dréau, J.-F. Roch, I. Diniz, A. Auffeves, D. Vion, D. Esteve, and P. Bertet, Phys. Rev. Lett. **107**, 220501 (2011).

[3] S. Probst, A. Bienfait, P. Campagne-Ibarcq, J. J. Pla, B. Albanese, J. F. Da Silva Barbosa, T. Schenkel, D. Vion, D. Esteve, K. Mølmer, J. J. L. Morton, R. Heeres, and P. Bertet, Appl. Phys. Lett. **111**, 202604 (2017).

[4] N. J. Lambert, A. Rueda, F. Sedlmeir, and H. G. L. Schwefel, Adv. Quantum Technol. **3**, 1900077 (2020).

[5] N. Lauk, N. Sinclair, S. Barzanjeh, J. P. Covey, M. Saffman, M. Spiropulu, and C. Simon, Quantum Sci. Technol. **5**, 020501 (2020).

[6] X. Fernandez-Gonzalvo, Y.-H. Chen, C. Yin, S. Rogge, and J. J. Longdell, Phys. Rev. A **92**, 062313 (2015).

[7] S. Probst, H. Rotzinger, S. Wünsch, P. Jung, M. Jerger, M. Siegel, A. V. Ustinov, and P. A. Bushev, Phys. Rev. Lett. **110**, 157001 (2013).

[8] Y.-H. Chen, X. Fernandez-Gonzalvo, and J. J. Longdell, Phys. Rev. B **94**, 075117 (2016).

[9] A. Tiranov, A. Ortu, S. Welinski, A. Ferrier, P. Goldner, N. Gisin, and M. Afzelius, Phys. Rev. B **98**, 195110 (2018).

[10] M. Businger, A. Tiranov, K. T. Kaczmarek, S. Welinski, Z. Zhang, A. Ferrier, P. Goldner, and M. Afzelius, Phys. Rev. Lett. **124**, 053606 (2020).

[11] H.-J. Lim, S. Welinski, A. Ferrier, P. Goldner, and J. J. L. Morton, Phys. Rev. B **97**, 064409 (2018).

[12] We will keep the term superhyperfine to designate the electron spin to ligand interaction even in absence of hyperfine structure as for the even isotopes of Er^{3+}.

[13] G. Liu and B. Jacquier, *Spectroscopic Properties of Rare Earths in Optical Materials*, Vol. 83 (Springer Science & Business Media, Berlin, Heidelberg, 2006).

[14] W. B. Mims, *Electron Paramagnetic Resonance*, edited by S. Geschwind (Plenum, New York, 1972).

[15] J. Hurrell and E. Davies, Solid State Commun. **9**, 461 (1971).

[16] O. Guillot-Noël, H. Vezin, P. Goldner, F. Beaudoux, J. Vincent, J. Lejay, and I. Lorgeré, Phys. Rev. B **76**, 180408(R) (2007).

[17] S. Probst, G. Zhang, M. Rančić, V. Ranjan, M. Le Dantec, Z. Zhong, B. Albanese, A. Doll, R. B. Liu, J. Morton, T. Chaneliè, P. Goldner, D. Vion, D. Esteve, and P. Bertet, Magn. Reson. Discuss. (2020), doi:10.5194/mr-2020-10.

[18] M. Mitsunaga, Phys. Rev. A **42**, 1617 (1990).

[19] B. Car, L. Veissier, A. Louchet-Chauvet, J.-L. Le Gouët, and T. Chanelière, Phys. Rev. Lett. **120**, 197401 (2018).

[20] L. G. Rowan, E. L. Hahn, and W. B. Mims, Phys. Rev. **137**, A61 (1965).

[21] S. Probst, H. Rotzinger, A. V. Ustinov, and P. A. Bushev, Phys. Rev. B **92**, 014421 (2015).

[22] Y. Q. Huan, J. M. Kindem, J. G. Bartholomew, and A. Faraon, in *Conference on Lasers and Electro-Optics*, OSA Technical Digest (Optical Society of America, 2019), paper JTu2A.26.

[23] S. R. Hastings-Simon, M. Afzelius, J. Minář, M. U. Staudt, B. Lauritzen, H. de Riedmatten, N. Gisin, A. Amari, A. Walther, S. Kröll, E. Cavalli, and M. Bettinelli, Phys. Rev. B **77**, 125111 (2008).

[24] R. M. Macfarlane, R. S. Meltzer, and B. Z. Malkin, Phys. Rev. B **58**, 5692 (1998).

[25] N. Kukharchyk, D. Sholokhov, O. Morozov, S. L. Korableva, A. A. Kalachev, and P. A. Bushev, New J. Phys. **20**, 023044 (2018).

[26] C. Li, C. Wyon, and R. Moncorge, IEEE J. Quantum Electron. **28**, 1209 (1992).

[27] S. P. Horvath, J. V. Rakonjac, Y.-H. Chen, J. J. Longdell, P. Goldner, J. P. R. Wells, and M. F. Reid, Phys. Rev. Lett. **123**, 057401 (2019).

[28] Y. Sun, T. Böttger, C. W. Thiel, and R. L. Cone, Phys. Rev. B **77**, 085124 (2008).

[29] O. Guillot-Noël, P. Goldner, Y. L. Du, E. Baldit, P. Monnier, and K. Bencheikh, Phys. Rev. B **74**, 214409 (2006).

[30] Y.-H. Chen, X. Fernandez-Gonzalvo, S. P. Horvath, J. V. Rakonjac, and J. J. Longdell, Phys. Rev. B **97**, 024419 (2018).

[31] B. A. Maksimov, V. V. Ilyukhin, Yu. A. Kharitonov, and N. V. Belov, Kristallografiya **15**, 1188 (1970).

[32] T. Böttger, C. W. Thiel, Y. Sun, and R. L. Cone, Phys. Rev. B **73**, 075101 (2006).

[33] ^{17}O with nonzero nuclear moment appears only as traces with 0.04% abundance.

[34] L. Kevan and R. N. Schwartz, *Time Domain Electron Spin Resonance* (John Wiley & Sons, New York, 1979).

[35] W. B. Mims, Phys. Rev. B **5**, 2409 (1972).

[36] W. B. Mims, J. Peisach, and J. L. Davis, J. Chem. Phys. **66**, 5536 (1977).

[37] B. Car, Study of spin dynamics around erbium ions for quantum memories, Ph.D. thesis, Université Paris-Saclay, 2019.

[38] L. Braunschweiler, A. Schweiger, J. Fauth, and R. Ernst, J. Magn. Reson. (1969) **64**, 160 (1985).

[39] H. Barkhuijsen, R. De Beer, B. Pronk, and D. Van Ormondt, J. Magn. Reson. (1969) **61**, 284 (1985).

[40] A. V. Astashkin, S. Dikanov, V. Kurshev, and Y. D. Tsvetkov, Chem. Phys. Lett. **136**, 335 (1987).

[41] See Supplemental Material at http://link.aps.org/supplemental/10.1103/PhysRevB.102.115119 for the complete set of 100 ions used for the calculation.